

# The structure and dynamics of the AC114 galaxy cluster revisited <sup>\*</sup>

Dominique Proust<sup>1</sup>, Irina Yegorova<sup>2</sup>, Ivo Saviane<sup>2</sup>, Valentin D. Ivanov<sup>2</sup>  
 Fabio Bresolin<sup>3</sup> John J. Salzer<sup>4</sup> and Hugo V. Capelato<sup>5,6</sup>

<sup>1</sup>*Observatoire de Paris-Meudon, GEPI, F92195 MEUDON, France*

<sup>2</sup>*European Southern Observatory, Alonso de Cordova 3107, Vitacura, Casilla 19001, Santiago de Chile 19, Chile*

<sup>3</sup>*Institute for Astronomy, 2680 Woodlawn Drive Honolulu, HI 96822 USA*

<sup>4</sup>*Department of Astronomy, Indiana University, 727 East Third Street, Bloomington, IN 47405, USA*

<sup>5</sup>*Divisão de Astrofísica, INPE-MCT, 12227-010 São José dos Campos, São Paulo, SP, Brazil*

<sup>6</sup>*Núcleo de Astrofísica Teórica, Universidade Cruzeiro do Sul, rua Galvão Bueno 868, CEP 01506-200, São Paulo, SP, Brazil*

Accepted date / Received date; in original form

## ABSTRACT

We present a dynamical analysis of the galaxy cluster AC114 based on a catalogue of 524 velocities. Of these, 169 (32%) are newly obtained at ESO (Chile) with the VLT and the VIMOS spectrograph. Data on individual galaxies are presented and the accuracy of the measured velocities is discussed. Dynamical properties of the cluster are derived. We obtain an improved mean redshift value  $z = 0.31665 \pm 0.0008$  and velocity dispersion  $\sigma = 1893_{-82}^{+73}$  km s<sup>-1</sup>. A large velocity dispersion within the core radius and the shape of the infall pattern suggests that this part of the cluster is in a radial phase of relaxation with a very elongated radial filament spanning 12000 km s<sup>-1</sup>. A radial foreground structure is detected within the central 0.5/h Mpc radius, recognizable as a redshift group at the same central redshift value. We analyze the color distribution for this archetype Butcher-Oemler galaxy cluster and identify the separate red and blue galaxy sequences. The latter subset contains 44% of confirmed members of the cluster, reaching magnitudes as faint as  $R_f = 21.1$  (1.0 magnitude fainter than previous studies). We derive a mass  $M_{200} = (4.3 \pm 0.7) \times 10^{15} M_{\odot}/h$ . In a subsequent paper we will utilize the spectral data presented here to explore the mass-metallicity relation for this intermediate redshift cluster.

**Key words:** galaxies: cluster – mass – metallicities – redshifts

## 1 INTRODUCTION

Redshift surveys of clusters of galaxies are needed to study their dynamical and evolutionary state. In clusters, the mean redshift is a key ingredient in deriving distances, allowing the study of matter distribution on very large scales. Analysis of the velocity distribution within clusters can lead to an estimate of the virial mass, constraining models of the dark matter content. Dynamical mass estimates complement measurements at other wavelengths, in particular those obtained through X-ray observations of clusters. However, discrepancies between optical, spectroscopic and X-ray mass estimators are often found (e.g., Girardi et al. 1998, Allen 2000, Cypriano et al. 2005). Virial mass estimates rely on

the assumption of dynamical equilibrium. X-ray mass estimates also depend on the dynamical equilibrium hypothesis and on the still not well-constrained intracluster gas temperature gradient (e.g., Leccardi & Molendi 2008) although it is much better established from both *Chandra* and *XMM* data analyses. Finally, mass estimates based on gravitational lensing are considered more reliable than the others (e.g., Mellier 1999) because they are completely independent of the dynamical status of the cluster. The drawback is that lensing cannot probe the mass profile beyond the virial radius of clusters. The discrepancies among the methods may come from the non-equilibrium effects in the central region of the clusters (Allen 1998).

In this paper, we build upon previous studies of the dynamical status of the cluster AC114 with the addition of a new set of velocities. The observations of radial velocities reported here are part of a program to study the mass-metallicity relation (MZR) in AC114 (Saviane et al.

<sup>\*</sup> Based on observations made with ESO Telescopes at the La Silla Paranal Observatory (Chile) under programme ID 083.A-0566.

2014, Saviane et al. 2015 *in preparation*), which is a powerful diagnostic of galaxy evolution, as first shown by Larson (1974). Note that the sensitivity of available instruments at 10m-class telescopes does not allow for the accurate determination of the MZR at the highest redshifts, but for AC114 at  $z \sim 0.32$  we are able to measure abundances reliably.

The AC114 cluster (R.A.=22h58mn52.3s Dec=-34°46′55″ J2000) is classified as Bautz-Morgan type II-III by Abell et al. (1989). It is the archetype object of the Butcher-Oemler effect with a higher fraction of blue, late-type galaxies than in lower redshift clusters, rising to 60% outside the core region (Couch et al. 1998, Sereno et al. 2010).

AC114 has 724 galaxies listed in *Simbad* in an area of  $\sim 10' \times 10'$ , and 585 of them are classified as emission-line galaxies. It has been observed several times. For example, Couch & Sharples (1987) derived 51 velocities (42 cluster members), Couch et al. (2001) with 51  $H_\alpha$  emitting cluster members, and more recently in the 2dF survey (Colless et al. 2003) and the 6dF survey (Jones et al. 2009). A total of 308 velocities are available in the NED database within a 10 arcmin radius, 348 within 20 arcmin and 414 within 30 arcmin. AC114 has a compact core dominated by a cD galaxy and a strong lensing power with several bright arcs and multiple image sources (Smail et al. 1995, Natarajan et al. 1998, Campusano et al. 2001). It is a hot X-ray emitter ( $kT = 8.0$  keV) with an irregular morphology. Below 0.5 keV, the X-ray emission is dominated by two main components: the cluster, roughly centered on the optical position of AC 114, and a diffuse tail, extending almost 400 kpc from the cluster center to the southeast. The cD galaxy is shifted with respect to the centroid of the X-ray emission but aligned in the general direction of the X-ray brightness elongation (see de Filippis et al. 2004). An extensive study of AC114 based on a multiwavelength strong lensing analysis of baryons and dark matter from Sereno et al. (2010) provided evidence of dynamical activity, with the dark matter distribution being shifted and rotated with respect to the gas, following the galaxy density in terms of both shape and orientation. Based on the lensing and X-ray data, they argue that the cluster extends in the plane of the sky and is not affected by the lensing over-concentration bias. As our observations increase by 32% the data available for this cluster, we expand the dynamical analysis of AC114 in the present paper. The mass-metallicity relation is developed in Saviane et al. (2014) and Saviane et al. (2015 *in preparation*).

We present in Sec. 2 the details of the observations and data reduction. In Sec. 3 we discuss the distribution and the velocity analysis of the cluster galaxies. Sec. 4 describes the kinematical structures of AC114 and Sec. 5 makes the analysis of the distribution in color and the Butcher-Oemler effect while in Sec. 6 we analyse the dynamical mass determinations of AC114. We summarize our conclusions in Sec. 7. We adopt here, whenever necessary,  $H_0 = 100h \text{ km s}^{-1} \text{ Mpc}^{-1}$ ,  $\Omega_M = 0.3$  and  $\Omega_\Lambda = 0.7$ .

## 2 OBSERVATIONS AND DATA REDUCTIONS

The observations were carried out in service mode with the VISible MultiObject Spectrograph (VIMOS; Le Fèvre et al. 2003) mounted on the Very Large Telescope, ESO (083.A-

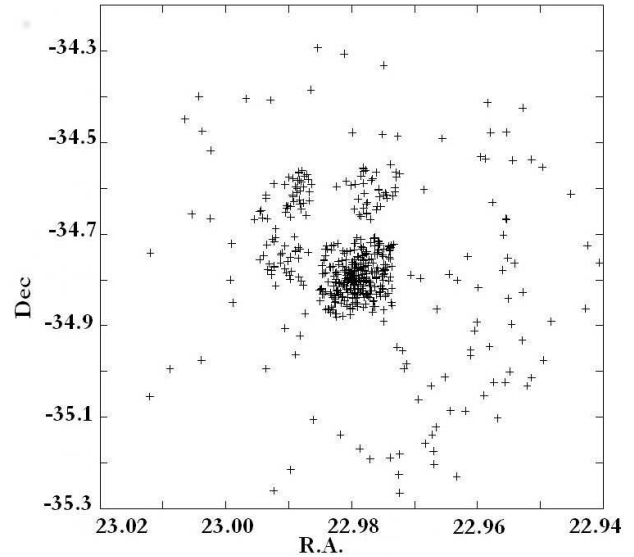


**Figure 1.** Map of the AC114 galaxies with observed velocities. The 4 central clumps are VIMOS observations at the VLT while galaxies spread in the field are from the literature.

0566). VIMOS is a visible light (360 to 1000 nm) wide field imager and multiobject spectrograph mounted on the Nasmyth focus B of UT3 Melipal. The instrument is made of four identical arms each with a field of view of  $7' \times 8'$ , and a  $0.205''$  pixel size. There is a  $\sim 2'$  gap between the quadrants. Each arm is equipped with 6 grisms providing a spectral resolution range from  $\sim 200 - 2500$  and with one EEV  $4k \times 2k$  CCD. Two dispersion modes were used: MR grating (spectral resolution of 580 for a  $1''$  slit, over 500 - 1000 nm spectral range) and HR-red grating (spectral resolution of 2500 for a  $1''$  slit, over 630 - 870 nm spectral range). The galaxy selection was made from the pre-imaging frames of the cluster. To construct the masks, initially, the SIMBAD catalogue was used without imposing any restriction criteria. As a first step we identified already known galaxies of the cluster. Then we selected the non-stellar objects in this region by eye in order to punch a maximum number of slits in each of the 4 quadrants. Such a visual inspection allows to discriminate between extended objects and stars.

The 14 awarded hours of observations were done on 2009 August, 16 and 21 and September 17, 21 and 25 (see Table 1). Execution time for each observing block was 60 minutes, including 22.5 minutes of overheads. Observing blocks were prepared for both MR and HR-red grisms. For each grism observing block was repeated seven times. The total integration time on target galaxies is 4.37 hours for each grism.

Figure 1 shows the projected map in R.A. and Dec of our program galaxies in AC114 out to a velocity  $cz = 120000 \text{ km s}^{-1}$ . Note that most of the objects in the central part represent 4 clumps corresponding to the 4 VIMOS quadrants of a VLT mask. The other galaxies spread in the field are objects already observed with velocities published in the literature.

The data reduction was carried out independently at ESO-Santiago and Paris-Meudon observatory in order to obtain wavelength and flux calibrated spectra. Thanks to the

□

**Table 1.** Observing blocks of AC114.

$OB_{ID}$	Date	OB start <sup>a</sup>	Exp. time <sup>b</sup>	Filter	Grism
382919	2009-09-17	02:37	2250	GG475	HR red
382920	2009-09-17	03:32	2250	GG475	HR red
382921	2009-09-17	04:11	2250	GG475	HR red
382922	2009-09-17	04:50	2250	GG475	HR red
382923	2009-09-17	05:28	2250	GG475	HR red
382924	2009-09-17	06:07	2250	GG475	HR red
382925	2009-09-21	03:54	2250	GG475	HR red
382926	2009-08-16	05:25	2250	GG475	MR
382927	2009-08-16	06:15	2250	GG475	MR
382928	2009-08-16	06:55	2250	GG475	MR
382929	2009-08-21	07:24	2250	GG475	MR
382930	2009-08-21	06:11	2250	GG475	MR
382931	2009-09-25	04:02	2250	GG475	MR
382932	2009-09-25	04:53	2250	GG475	MR

<sup>a</sup> beginning of the observation block, UT time<sup>b</sup> exposure time of the science part, in seconds

double reduction of the data, we could compare the quality of the results. At ESO-Santiago we used the VIMOS pipeline to reduce the data. We reduced separately the data taken with the grism HR red and MR. Each scientific frame was bias subtracted and flat field corrected, the cosmic rays were removed, and sky emission lines subtracted (the same procedure was done for the standard stars). The spectra were wavelength calibrated and seven frames for each VIMOS quadrant were combined. This gave us  $S/N = 20$  per pixel on the average at the continuum level on the final spectra. Since the continuum of most of the galaxies is too weak we did not use the spectra extracted by the pipeline. Instead, we extracted one-dimensional spectra with MIDAS.

At Meudon, we independently reduced the data with the MULTIREDD package (Le Fèvre et al. 1995) of IRAF<sup>1</sup> performing the following steps in sequence for each slit:

- Extract small 2D postage-stamp images corresponding to one slit from the two dimensional spectra of the object and the corresponding wavelength calibration and flat field from the full  $4k \times 2k$  pixel images.

- For each two-dimensional spectrum correct for flat field (pixel to pixel variation) and subtract sky emission: the sky is fitted with adjustable low-order polynomials, and subtracted along the slit for each wavelength element. A treatment of the zero-order position was also added: areas on the two-dimensional spectra with a zero order could be corrected independently from the rest of the spectrum, if needed.

- Combine all the corrected two-dimensional spectra of a given object with average or median scheme using sigma-clipping rejection. This removes most of the cosmic-ray events, although in some circumstances, the brightest events can still partially remain.

- Extract a one-dimensional spectrum of the arc-lamps and cross-correlate with a reference arc-lamp spec-

trum to produce an initial wavelength solution. The fit was then adjusted, if necessary. This produces a unique pixel/wavelength transformation for each slit.

- Extract a one-dimensional spectrum from the corrected two-dimensional spectrum for each object of interest in the slit by averaging along the wavelength axis.

- Wavelength and flux calibrate the one-dimensional object spectrum. We observed the F-type standard star LTT1788 ( $V = 13.16$ ,  $B-V = +0.47$ ) and the DA-type LTT7987 ( $V = 12.23$ ,  $B-V = +0.05$ ) from Hamuy et al. (1992, 1994).

- Plot the corrected and calibrated one-dimensional spectrum and display all the corrected two-dimensional spectra together with the averaged two-dimensional spectrum. Line identification for redshift measurement can then proceed.

Because of the lack of CCD photometry for this cluster, we collected UK-J  $B_j$  and ESO-R or POSS-I E  $R_f$  magnitudes from superCOSMOS (Maddox et al. 1990a, 1990b); The photometric accuracy of these data is typically 0.3 mag with respect to external data for  $m > 15$ . Colours (B-R or R-I) are externally accurate to 0.07 mag at  $B_j = 16.5$  rising to 0.16 mag at  $B_j = 20$ .  $B_j$  and  $R_f$  magnitudes are listed in Table 2. Looking at this table, the faintest objects for which superCOSMOS provides an apparent magnitude estimate have magnitudes  $B_j = 22.6$  and  $R_f = 21.1$ . However it is also clear that luminosities are not available for roughly fifty percent of our targets. To overcome this limitation, we obtained a relation between the integrated flux of our spectra and the  $R_f$  magnitude, and then the relation was applied to get a first estimate of the  $R_f$  magnitude for objects that do not have a luminosity estimate.

The flux integral was computed simply as  $\Sigma f \times \delta\lambda$ , where  $f$  is the flux in units of  $10^{-16}$  erg  $\text{cm}^{-2} \text{sec}^{-1} \text{\AA}^{-1}$  and  $\delta\lambda = 2.6 \text{\AA}$  is the spectral bin. The flux integral was limited to the common spectral range of the spectra, which is from  $4897.5 \text{\AA}$  to  $9785.5 \text{\AA}$ . The relation between the integrated flux and  $R_f$  is shown in Fig. 2. Assuming that the relation is linear, with a preliminary fit we found that the slope of the regression is  $\sim 2.7$ , which suggests that our integrated flux is

<sup>1</sup> IRAF is distributed by the National Optical Astronomy Observatories, which are operated by the Association of Universities for Research in Astronomy, Inc., under cooperative agreement with the National Science Foundation.

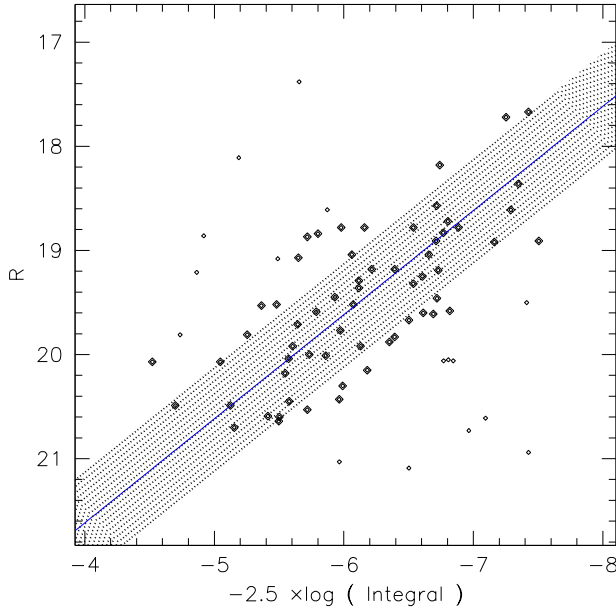


**Figure 2.** Relation between  $R_f$  magnitudes and the flux integral described in the text. Objects identified by larger symbols were considered in the linear regression, which is shown by the straight line. The shaded area represents the  $\pm 1\sigma$  dispersion around the fit.

close to what is measured by the R-band photometry. Therefore we imposed the relation to be  $R_f = -2.5 \log f + R_0$  and we found  $R_0 = 25.62$ , with a dispersion of 0.51 dex around the fit.

The dispersion is quite satisfactory for an order-of-magnitude estimate of galaxian luminosities, and it is likely due to object-to-object variations in slit losses, night-to-night differences in the flux calibration of the VIMOS spectra, and variable sky transparency in the course of the observations.

Using the relation above, for each galaxy an  $R_{comp}$  magnitude can be computed, and luminosity distributions can be produced. In Fig. 3 we show such distributions for 25 galaxies that already have a spectrum in the literature as flagged by an entry in the NED database<sup>2</sup>, and for 138 galaxies added with the present work. No selection was done; this work covers a larger area than older datasets. The apparent magnitude distribution of galaxies with existing spectra turns over at  $R_{comp} \sim 19$  while that of our new sample keeps growing down to  $R_{comp} \sim 20$ . Below  $R_{comp} \sim 19$  the literature sample thus suffers from incompleteness compared to our new sample, which reaches  $\sim 1$  magnitude deeper than existing data. The mismatch between the  $R_f$  and  $R_{comp}$  sensitivity/integration bands may also contribute to the dispersion in the relation.

In order to study the completeness of our catalogue, we compared it to the corresponding superCOS-

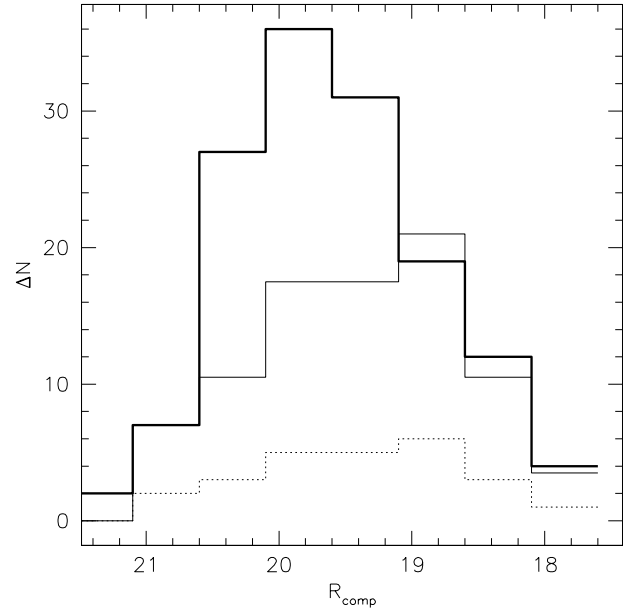


**Figure 3.** Luminosity distribution of galaxies with existing spectra (dotted-line histogram) and of galaxies added by the present study (thick-line histogram). To better compare the two samples, the thin-line histogram has been scaled from the dotted-line one so that the sum of counts in the three brightest bins is the same as that of the thick-line histogram. This scaling factor of 3.5 almost coincides with the ratio of the area surveyed by us and the area defined by literature data. R-band magnitudes were computed as described in the text.

MOS plate<sup>3</sup> (Hambly et al. 2001) as our faintest program galaxies are close to the superCOSMOS limiting magnitude ( $\simeq B_j = 23.0$  and  $R_f = 21.5$ ). In the core radius  $R_c = 1.02$  arcmin (0.27/h Mpc see Couch et al. 1987), all of the 8 galaxies have velocities. In the Abell radius computed above  $R_{Abell} = 5.431$  arcmin (1.44/h Mpc), 109 out of 173 galaxies (63%) have velocities and in the virial radius  $R_v = 3.0/h$  Mpc (see Couch et al. 2001) 340 out of 724 galaxies (47%) have velocities.

Radial velocities have been determined using the cross-correlation technique (Tonry 1979) implemented in XCSAO task of the RVSAO package (Kurtz 1991, Mink 1995) with spectra of radial velocity standards of late-type stars (Pickles 1998) and previously well-studied galaxies (Pickles 1985). The values of their R statistics (defined as the ratio of the correlation peak height to the amplitude of the antisymmetric noise) are listed in Table 2 along with the measured velocities and their formal uncertainties. For spectra with  $R < 3.0$  the measured velocity was considered unreliable and was not used, except for emission-line objects where the velocity was obtained using the EMSAO task implemented in the RVSAO package.

<sup>2</sup> The NASA/IPAC Extragalactic Database (NED) is operated by the Jet Propulsion Laboratory, California Institute of Technology, under contract with the National Aeronautics and Space Administration.

<sup>3</sup> This research has made use of data obtained from the superCOSMOS Science Archive, prepared and hosted by the Wide Field Astronomy Unit, Institute for Astronomy, University of Edinburgh, which is funded by the UK Science and Technology Facilities Council.

A total of 176 of the 200 observed spectra had S/N high enough to measure a useable velocity. Of these, 169 were galaxies, while 7 of them were found to be stars. Note that for 4 galaxies we derived two independent redshifts: object 45 in quadrant 1 with redshifts respectively 0.34461 and 0.35159, object 1 in quadrant 2 (0.25782 and 0.33069), and in quadrant 4 object 9 (0.25733 and 0.29095) and object 55 (0.17199 and 0.31776); after a visual inspection, these 4 targets seem to be composed by two objects in the line of sight. With our observations, we increase the number of galaxies with velocities in the field of AC114 by 32%. Most of these are situated in the central region of the cluster. The new redshift values with their individual error measurements are published in Table 2 and correspond to the highest R-value obtained from the cross-correlations. We have constructed a velocity catalogue for AC114 with a total of 524 galaxies, where 169 are new measured velocities and 355 galaxies are from NED.

The contents of Table 2 are as follows:

- (i) number of the object in each quadrant from slit position;
- (ii) right ascension (J2000);
- (iii) declination (J2000);
- (iv) UK-J  $B_j$  magnitude from superCOSMOS (Maddox et al. 1990a,b);
- (v) ESO-R or POSS-I E  $R_f$  magnitude from superCOSMOS (Maddox et al. 1990a,b);
- (vi)  $R_{comp}$  computed magnitude from spectra;
- (vii) redshift;
- (viii) redshift error;
- (ix) R value from the cross-correlation (Tonry 1979);
- (x) notes.

Figure 4 shows the wedge diagrams in R.A. and Dec for both set of observed and NED galaxies out to  $120000 \text{ km s}^{-1}$  with 468 galaxies; in the  $\sim 10' \times 10'$  central area of the cluster we have 189 velocities. Among the 169 velocities of table 2, 26 galaxies have previously published velocities listed in NED. Figure 5 shows the velocity comparison for these 26 galaxies. It can be seen that NED velocities tend to be larger than those measured in this work, although this is just a  $0.7\sigma$  effect. The dispersion is larger than our measurement errors, which is likely due to the non-homogeneity of the NED sample. We note a large velocity difference for the galaxy 56 in quadrant 4 of our table 2 ( $98377 \text{ km s}^{-1}$  and  $97642 \text{ km s}^{-1}$  from Couch et al. 1998). As our correlation coefficient is weak ( $R=3.31$ ) and our velocity error large ( $132 \text{ km s}^{-1}$ ) we give preference to their value.

Figure 6 shows the sky distribution of emission-line galaxies (blue dots) and of passive galaxies (red dots) in our newly measured spectra for six different redshift ranges. There are 21 emission-line galaxies at the redshift of AC114 out of a total of 86 cluster members. The bottom panel shows that the fraction of emission-line galaxies has a dip at the redshift of AC114, and that these galaxies tend to avoid the cluster center. Error bars in that panel show the 95% confidence limits, calculated according to formula 3.27 in Feigelson & Babu (2013).<sup>4</sup> At such a redshift, all important

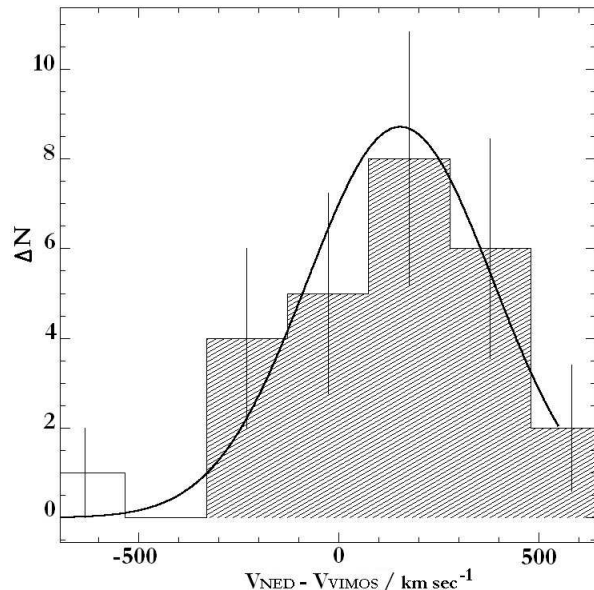


**Figure 5.** Velocity comparison between 26 velocities in common with the present work (VIMOS) and the NED database. After discarding the outlying galaxy with a very low NED velocity, the  $v_{\text{NED}} - v_{\text{VIMOS}}$  distribution (shaded histogram) resembles a Gaussian one, albeit with a slight excess on the small values side. Velocity differences are distributed around the average  $154 \text{ km s}^{-1}$  with a dispersion of  $232 \text{ km s}^{-1}$ . The normal distribution with these parameters and the same area of the histogram is shown by the solid curve.

emission lines still fall in the optical range, and the universe is  $\simeq 70\%$  its current age, so we can expect a factor 1.4 increase in  $Z$  since that time, or 0.14 dex in  $[m/H]$  (Gullieuszik et al. 2009, Leaman et al. 2013). A discussion concerning the mass-metallicity relation from this new set of emission-line galaxies is developed in Saviane et al. (2014) and Saviane et al. (2015 *in preparation*).

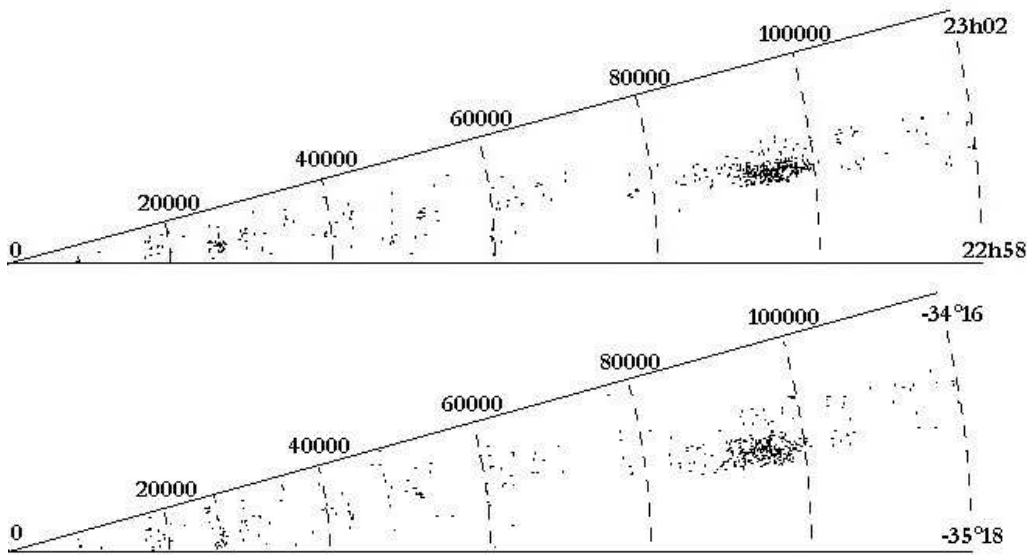
### 3 VELOCITY ANALYSIS

Figure 7 shows the redshift distribution of the spectroscopic sample within an area of  $\simeq 1.0$  square degree centered on AC114. The large central peak at  $z \sim 0.315$  corresponds to the main cluster. Other structures are seen, most for  $z \leq 0.25$ , as well also for  $z \sim 0.41$ . Note the important contamination by fore- and background objects along the line of sight: 45% of the galaxies in our redshift catalogue are non-members of AC114. Couch & Sharples (1987) found it to be 18% from 51 galaxies observed in a field of only  $5 \times 5$  arcmin. In the same field we have 114 redshifts with a contamination rate of 23% which is not significantly different.

We used the ROSTAT routines (Beers et al. 1990) to analyze the galaxy velocity distribution of AC114. The

so that  $z_{\alpha/2} = 1.96$  in the formula. No confidence intervals were computed for the lowest and the highest redshift bin where the Gaussian approximation to the binomial distribution does not hold.

<sup>4</sup> We have assumed that for our relatively large samples, the binomial distribution can be approximated by a normal distribution,



**Figure 4.** Wedge diagrams in R.A. and Dec for both the newly observed and literature galaxies until  $120000 \text{ km s}^{-1}$ .

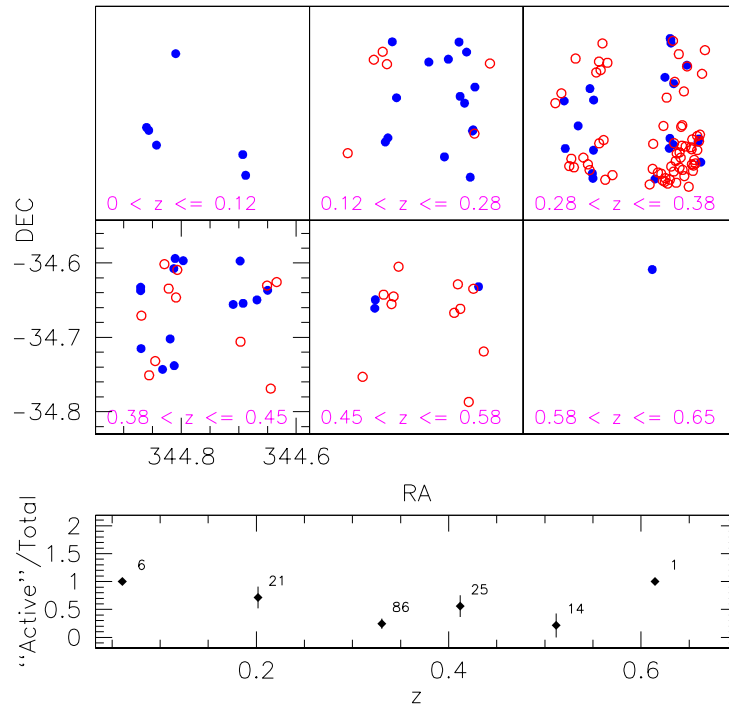


**Figure 6.** The top panels show the sky distribution of emission-line galaxies (blue dots) and of passive galaxies (red dots) for six redshift groups. The bottom plot shows the ratio of emission-line-to-total number of galaxies as a function of redshift. Error bars represent the 95% confidence limits, and numbers near each point give the total number of galaxies for each redshift interval.

dominant kinematical structure shown on Figure 7 contains 265 galaxies between  $z=0.295$  and  $z=0.34$ , including 77 new velocities. The rest-frame velocities  $v = c(z - \bar{z})/(1 + \bar{z})$  range from  $-4312 \text{ km s}^{-1}$  to  $3955 \text{ km s}^{-1}$  at  $\bar{z} = 0.31665_{-0.00082}^{+0.00072}$ . The large rest-frame dispersion comes out as  $\sigma = 1893_{-82}^{+73} \text{ km s}^{-1}$  suggesting that the cluster could be in a radial phase of relaxation with the presence of fore and background structures. The very elongated radial fil-

ament spanning  $12000 \text{ km s}^{-1}$  seen in Figure 4 is a manifestation of the familiar *finger-of-god* effect due to this large internal dispersion velocity. Note that all the normality tests included in the ROSTAT package fail to reject the null hypothesis of a Gaussian distribution for this sample.

We can deduce that AC114 has an Abell radius defined by  $R_{Abell}(\text{arcmin}) \sim 1.72/\bar{z}$ , which gives  $R_{Abell} = 5.431 \text{ arcmin}$  ( $1.44/h \text{ Mpc}$ ) with an angular size distance

of 909/h Mpc and a scale of 264.54 Kpc arcmin<sup>-1</sup> (and a luminosity distance of 1560/h Mpc from the mean redshift corrected to the Reference Frame defined by the 3K CMB). Note that Couch & Sharples (1987) found a dispersion  $\sigma = 1649_{-156}^{+217}$  km s<sup>-1</sup> from a set of 42 galaxies in a square region of 5 × 5 arcmin (1.32 × 1.32/h Mpc) and Mahdavi & Geller (2001) with  $\sigma = 1660_{-106}^{+128}$  km s<sup>-1</sup> within a radius of 4.45 arcmin (1.18/h<sub>50</sub> Mpc). Finn et al. (2004) give a dispersion of  $\sigma = 1390$  km s<sup>-1</sup> with  $r_{200} = 1.87/h_{100}$  (9.54 arcmin) and Just et al. (2010) obtain similar values with  $r_{200} = 3.98/h_{70}$  Mpc radius with 196 galaxies:  $\bar{z} = 0.31500$  and  $\sigma = 1889_{-74}^{+81}$  km s<sup>-1</sup>. Figure 8 shows the rest-frame velocity histogram between 89000 and 101000 km s<sup>-1</sup> and the gaussian with  $\sigma = 1893$  km s<sup>-1</sup>.

The brightest cluster member (BCG; R.A.=22h58mn48.4s Dec=-34°48'08" J2000) has a redshift  $z = 0.31691 \pm 0.00029$ , very close to the average redshift of the cluster. This galaxy is not infrared-luminous compared with other massive early-type galaxies, suggesting that the cluster environment has little influence on the infrared luminosities of these galaxy as discussed by Martini et al. (2007).

## 4 KINEMATICAL STRUCTURES

### 4.1 Method

In order to get more precise identifications of these structures, we applied the gap technique thoroughly discussed by Katgert et al. (1996). These consists in fixing a maximum allowed gap size in the rest-frame peculiar velocity space as a condition for galaxies to belong to a given structure. Adami et al. (1998) pointed out that gap sizes should not be kept constant, but should depend on the size  $N_S$  of redshift sample since it is more likely to find large gaps in sparse data-sets than in the richer ones, whereas a fixed gap would tend to overestimate the number of groups when  $N_S$  is small. Based on simulations of Gaussian distributions with varying number of objects they define the *density gap* such that:

$$\Delta v_{max} = \delta_{gap} \cdot f(N_S) \quad (1)$$

with

$$f(N_S) = (1 + \exp(-(N_S - 6)/33)) \quad (2)$$

and  $\delta_{gap} = 500$  km s<sup>-1</sup>. In redshift space this translates to:

$$\Delta z_{max} = (500/c)(1 + z_{cl})f(N_S) \quad (3)$$

where  $z_{cl}$  is the mean redshift of the candidate structure and  $c$  is the speed of light in km s<sup>-1</sup>.

We ran this gapping procedure for each of the candidate structures observed in the histogram displayed in Figure 7. Following Lopes et al. (2009; see also Ribeiro et al. 2013) we start by first looking at their densest central region, assumed to be circular with 0.5/h Mpc radius. We assume the central position of the main cluster as the initial guess for the calculations and further refine the central position of each candidate structure after collecting the galaxies belonging to the  $z$ -groups associated to it and re-starting the whole procedure. The  $z$ -groups detected by the gapping have their mean (bi-weighted) redshift  $\bar{z}_\nu$  estimated and ranked accordingly to their distance to the nominal redshift of the

candidate kinematical structure,  $\delta_{\bar{z}} \equiv |\bar{z}_\nu - z_{cl}|$ , with the most nearby being identified to it, providing:

$$\delta_{\bar{z}} \leq \Delta v_{max}(1 + z_{cl})/c \quad (4)$$

with  $\Delta v_{max} = 1000$  km s<sup>-1</sup>, allowing for the uncertainties and biases affecting the estimate of  $z_{cl}$ . Normally only one group survives this criteria and we then assume  $z_{cl} = \bar{z}_\nu$  for this candidate structure. A new central sky position is calculated from the positions of the galaxies belonging to this  $z$ -group and the whole procedure is iterated once. Next we search for the extreme values  $z_{min}$ ,  $z_{max}$  of the redshift distribution of the structure and then select all galaxies within 2.5/h Mpc from its center according to:

$$|z_i - z_{cl}| \leq \max\{z_{cl} - z_{min}, (z_{max} - z_{cl})\} \quad (5)$$

We gauge the significance of the kinematical structures identified so far by bootstrap re-sampling the full redshift distribution found inside the 0.5/h Mpc radius around its center and re-applying the whole procedure exactly as before. We do that  $N_{boot} = 1000$  times and then check the probability of detection of the group:

$$p(\bar{z}_\nu) = \frac{N_+(\bar{z}_\nu)}{N_{boot}} \quad (6)$$

where  $N_+(\bar{z}_\nu)$  is the number of positive detections for the group  $\bar{z}_\nu$ .

Finally, in order to reject possible interloper galaxies we apply the "shifting gapper" technique (Fadda et al. 1996, Lopes et al. 2009), which consists on the same gapping procedure as described above but applied within radial bins of width  $\geq 0.4/h$  Mpc containing at least 15 galaxies. The maximum redshift gap is now fixed at:

$$\Delta z_{max} = (300/c)(1 + z_{cl})f(N_S) \quad (7)$$

and we require that the mean redshift of the group does not deviate from  $z_{cl}$  by more than  $\delta_{\bar{z}} \leq 300(1 + z_{cl})/c$ . If no  $z$ -group is found satisfying these requirements the procedure stops and the aperture radius of the structure is identified to the internal radius of the bin.

### 4.2 Results

We limited our analyses to the interval  $0.25 \leq z \leq 0.5$ , which contain the main peak due to AC114 as well as neighbors foreground and background structures which may or may not interact with the main cluster. Table 3 displays the main parameters of the kinematical structures we have found. Besides the main cluster AC114, which dominates Figure 7, we have been able to detect two others secondary structures although at low levels of significance. Figure 9 (upper panel) shows the resulting redshift distribution of these structures and Figure 9 (lower panel) shows with different symbols the projected positions of their galaxies.

The foreground structure AC114 01 seems to be much more relevant for our discussion on the evolutionary status of the main cluster. Although being detected as a redshift group of only 4 galaxies within the central 0.5/h Mpc radius, and as so suggesting to be a mere statistical fluctuation of the phase space distribution of galaxies, we argue that, besides the 77% of chances of detection (on 1000 bootstrap trials), this structure is still recognizable as a redshift group at the same central redshift value (within  $c\delta_z \sim 300$  km s<sup>-1</sup>) at

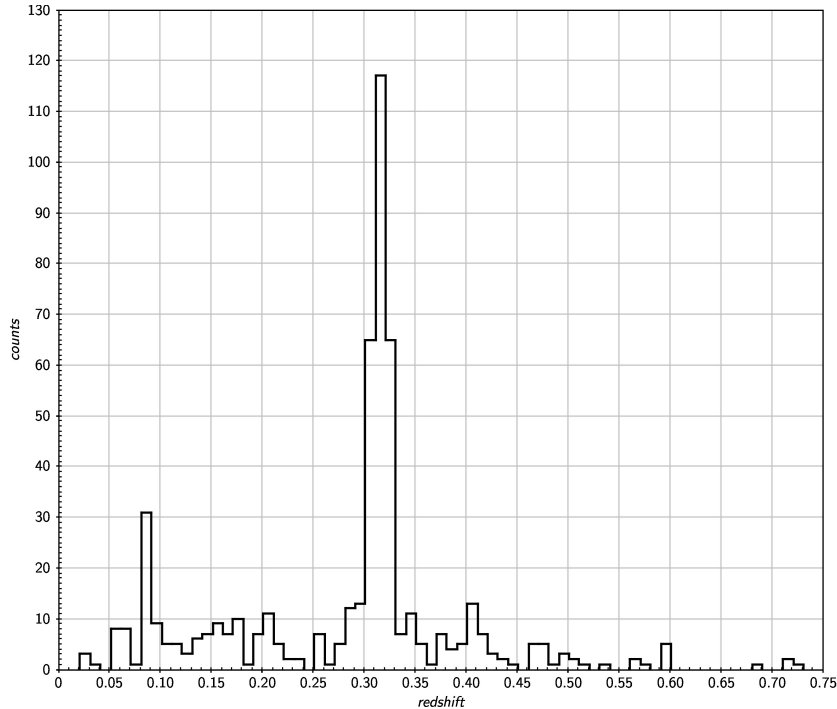


**Figure 7.** The redshift distribution within an area of  $\sim 1.0$  square degrees centered on the AC114 cluster.

projected distances far from its very center. In fact the shifting gapper was able to follow it out to  $3.03/h_{73}$  Mpc which is  $\sim 90\%$  of the limiting radius  $2.5/h$  Mpc. Given their proximity in redshift space - almost certainly reflecting their relative space configuration - it is very difficult to completely disentangle the redshift distribution of AC114 01 from that of the main cluster. Nevertheless we have been able to make roughly estimates of the population of interloper galaxies of AC114 01. In principle these should be constituted else by galaxies in their way of being torn from AC114 01 by the main cluster or by galaxies already dynamically linked to it.

Finally, as it can be seen from Figure 9 (lower panel), the galaxies taking part of AC114 02 are sparsely distributed background to the main AC114 suggesting else they do not constitute a bound structure, or else the sky region it occupies has suffered of a bad sampling.

Note that if the relaxation occurs in two or more clusters in the line of sight, supporting evidence for this is extremely difficult to recognize with the existing data. Czoske et al. (2001,2002) showed that the redshift distribution of the cluster Cl0024+17 ( $z = 0.395$ ) is bimodal with a large primary component and a second foreground one, separated by  $v = 3000 \text{ km s}^{-1}$ , suggesting that the system is undergoing a radial high velocity collision (note that both AC114 and Cl0024+17 show Butcher-Oemler effect, see the next section). The Cl0024+17 bimodality is confirmed by Zuhone et al. (2009) using a high-resolution N-body/hydrodynamics simulation of such a collision. In the case of AC114, comparing Figure 7 with Figs. 1 and 3 of Czoske et al. (2002) suggests the foreground structure mentioned above as a distinct grouping although the foreground one of Cl0024+17 is much more clearly delineated.

Following Rood et al. (1972), Kent & Gunn (1982) and more recently Czoske et al. (2002), we have constructed the

AC114 pseudo-phase diagram by plotting the redshift for each galaxy versus its projected distance from the cluster center on Figure 10. The well-sampled part of AC114 corresponds to the very central part of the cluster Cl0024+17 extending 5 arcmin on the Figure 2 of Czoske et al. (2002). The distribution of the galaxies in the main peak is symmetrical with respect to the central redshift, whereas the distribution of the foreground galaxies is evidenced at a rest frame velocity of  $\simeq -5000 \text{ km s}^{-1}$  at radii until 7 arcmin, but turns out towards smaller relative velocities to merge with the main distribution at smaller projected distances. The background galaxies velocity at a rest frame of  $\simeq +4000 \text{ km s}^{-1}$  are much more widely dispersed and we cannot rule out a connection with AC114; it seems more likely that they are part of the surrounding field galaxy population. Note the “trumpet shaped” region extending horizontally from the cluster center. The infall pattern around rich clusters of galaxies has been studied by Regos & Geller (1989) by constructing an analytic model for the distribution of galaxies around a cluster core in redshift space. From their Figure 6-b) showing the redshift as a function of the angular separation on the sky from the cluster center, the high-density caustic surfaces which define the infall pattern show this characteristic trumpet shape. This shape is interpreted by these authors as the collapsing structure in which galaxies trace the matter distribution on the scale of the infall region and moreover, the caustics have a dependence on  $\Omega_0$ . Such model has been tested by Regos & Geller (1989) for the rich clusters A539, Coma, A2670, A1367 and by Reisenegger et al. (2000) for the Shapley supercluster. Diaferio & Geller (1997) interpreted this trumpet shape as outlining the escape velocity profile rather than caustics due to the infall pattern. The appearance of Figure 10 supports the reality of the foreground structure as it appears to lie mostly outside of the



lower caustic. However, it is situated close to the limit of the virial radius of AC114. With a more complete set of velocities one could perhaps resolve definitively the dynamical status of AC114 and its immediate environs.

We also applied the method developed by Dressler & Shectman (1988) with the  $\delta$  parameter to test for kinematical structures defined as:

$$\delta^2 = (11/\sigma^2[(\bar{v}_{local} - \bar{v})^2 + (\sigma_{local} - \sigma)^2]) \quad (8)$$

where  $v_{local}$  and  $\sigma_{local}$  are the local velocities and dispersions calculated from the 10 nearest neighbors of each galaxy within the  $r_{200}$  radius which defines the limits of the virialized cluster from its redshift and velocity dispersion (i.e., with average density 200 times the critical one, see e.g., Diaferio et al. 2001, Finn et al. 2004):

$$r_{200} = 1.73 \frac{\sigma_{v,cl}}{1000 \text{ km s}^{-1}} \frac{1}{\sqrt{\Omega_\Lambda + \Omega_o(1+z_{cl})^3}} / h \text{ Mpc} \quad (9)$$

In random redistributions of the measured galaxy velocities and positions, with  $r_{200} \simeq 2.78/h$  Mpc we found the sum of the  $\delta$  values to be equal to or larger than the observed value with a frequency of  $P_\delta = 0.138$ . This value is too marginal to conclusively verify the existence of substantial substructures. With  $\sigma_{v,cl} = 2025 \text{ km s}^{-1}$  Martini et al. (2007) give  $r_{200} \simeq 4.25/h_{70}$  Mpc and  $P_\delta = 0.156$ . Just et al. (2010) give  $r_{200} = 3.98/h_{70}$  Mpc while Couch et al. (2001) use a value  $r_v = 3.0/h_{100}$  Mpc.

## 5 GALAXY COLOR DISTRIBUTION AND THE BUTCHER-OEMLER EFFECT

As UK-J  $B_j$  and ESO-R or POSS-I-E  $R_f$  magnitudes are available from superCOSMOS (Maddox et al. 1990a, 1990b) a color-magnitude diagram  $B_j - R_f$  versus  $R_f$  for AC114 member galaxies identified from their redshift is shown in Figure 11 (fore - and background objects have been removed). Note that plusses and crosses correspond respectively to absorption and emission lines galaxies observed by Couch & Sharples (1987), while squares and stars correspond to absorption and emission lines galaxies of the present work and from various literature sources listed in NED, including the 6 AGN from Martini et al. (2006). The excess of blue galaxy cluster members ranging from 16 to 30% is known as the Butcher-Oemler (BO) effect (Butcher & Oemler 1978). As discussed by Couch & Sharples (1987), a “red” galaxy sequence is defined with objects having  $B_j - R_f \geq 2.0$ . We identify this galaxy sequence extending to  $R_f = 21.5$  distributed along the regression line on the top of the Figure 11 with  $B_j - R_f = -0.0435B_j + 3.169$ . This sequence is well separated from the “blue” galaxy area, where all emission-lines galaxies are present. The ratio of emission/absorption lines galaxies belonging to AC114 is 19% in Couch & Sharples (1987) and 24% in the present work. No obvious dynamical difference is seen between the red and blue populations as the red one with 47 objects gives  $\bar{z} = 0.31757$  with  $\sigma = 2019_{-103}^{+115} \text{ km s}^{-1}$  and the blue one with 37 objects gives  $\bar{z} = 0.31723$  with  $\sigma = 1835_{-121}^{+108} \text{ km s}^{-1}$ .

As quoted in Couch & Sharples (1987) BO cluster member galaxies represent 36% of the total population in AC114, while Martini et al. (2007) found a ratio of 26% brighter than  $M_R = -20$  and we have 44% of blue objects in the present

work. Such a discrepancy is a consequence of our galaxy sample, where most of them are located in the central region of AC114. It is also an effect of the larger number of galaxy cluster members with available photometry as well as the spectroscopy limiting magnitude of our sample which reaches magnitudes as faint as  $R_f = 21.1$  (i.e., more than one magnitude fainter than the previous studies).

## 6 DYNAMICAL MASS DETERMINATIONS OF AC114

The mass of a cluster can be computed in several ways (Serenio et al. 2010). However, dynamical methods are based on the assumption that the cluster is close to equilibrium. In the case of AC114, as the foreground structure overlaps partially the main one, we considered the cluster as a whole. Assuming that galaxies are test particles orbiting in a dark matter spherical potential (Binney & Tremaine 1987), the expression for the virial mass of a cluster is:

$$M_v = \frac{3\pi}{2} \frac{\sigma^2 R_{Pv}}{G} - C_{Pr} \quad (10)$$

Here  $R_{Pv}$  is the projected virial radius of  $N$  observed galaxies and

$$R_{Pv} = \frac{N(N-1)}{\sum_{i>j} R_{ij}^{-1}} \quad (11)$$

where  $R_{ij}$  is the projected distance between two galaxies given by  $i$  and  $j$ .  $C_{Pr}$  is a surface term which accounts that the system is not entirely enclosed in the observational sample with:

$$C_{Pr} = 4\pi r_{200}^3 \frac{\rho(r_{200})}{\int_0^{r_{200}} 4\pi r^2 \rho dr} \left( \frac{\sigma_r(r_{200})}{\sigma(<r_{200})} \right)^2 \quad (12)$$

where  $\sigma_r(r_{200})$  is the radial velocity dispersion at  $r_{200}$  and  $\sigma(<r_{200})$  is the enclosed total velocity dispersion within  $r_{200}$  (Girardi et al. 1998). On average, for clusters observed within a radius of 1.5/h Mpc, this correction is  $\simeq 16\%$  (Biviano et al. 2006). The cluster AC114 has a redshift  $z = 0.31665$  and a line-of-sight dispersion  $\sigma = 1893 \text{ km s}^{-1}$  with  $N = 265$  galaxies cluster members between 88500 and 102000  $\text{km s}^{-1}$ . We obtain:  $M_{200} = (4.3 \pm 0.7) \times 10^{15} M_\odot / h$  enclosed within the virial radius. Our mass estimate is close to that derived by Serenio et al. (2010). For a mean redshift  $z = 0.3153$  and a velocity dispersion  $\sigma = 1900 \text{ km s}^{-1}$  they obtained  $M_{200} = (3.4 \pm 0.8) \times 10^{15} M_\odot / h$ .

The mass estimate can also be computed from the 3D intrinsic velocity dispersion  $\sigma_v$  within  $r_{200}$  (Biviano et al. 2006) with:

$$M_v \equiv (1.5 \pm 0.02) \left( \frac{\sigma_v}{10^3 \text{ km s}^{-1}} \right)^3 \times 10^{14} M_\odot / h \quad (13)$$

The intrinsic velocity dispersion  $\sigma_v$  is corrected from the velocity dispersion profile following Figure 4 of Biviano et al. (2006) which gives for AC114  $M_v = (5.4 \pm 0.7 \pm 0.6) \times 10^{15} M_\odot / h$ . Here the first error is statistical, and the second one reflects the theoretical uncertainty on the relation (Serenio et al. 2010). Serenio et al. (2010) use this method to find a similar mass:  $M_v = (4.8 \pm 0.8 \pm 0.6) \times 10^{15} M_\odot / h$ . Note that Serenio et al. (2010) derived another mass estimate using the concentration parameter from a triaxial radius  $r_{200}$  such that the mean density contained within an

□

**Table 2.** Positions, photometric data and velocities for galaxies of AC114. The R column is the correlation peak height to the amplitude of the antisymmetric noise (see text for explanation).

Gal.	R.A. (J2000)	Dec. (J2000)	$B_j$ mag	$R_f$ mag	$R_{\text{comp}}$ mag	redshift	error	R	notes
Quadrant 1									
1	22 59 20.70	-34 42 24.6			20.0	0.39852	0.00030	3.50	em:H $\alpha$ ,S1
2	22 59 31.37	-34 42 28.4			20.5	0.35306	0.00018		em:OII,H $\beta$ ,2OIII,H $\alpha$ ,S1
3	22 59 33.46	-34 42 39.8			18.0	0.05717	0.00011		em:H $\beta$ ,2OIII,H $\alpha$ ,S1
5	22 59 32.31	-34 42 58.2	20.2		20.1	0.05842	0.00009		em:H $\beta$ ,2OIII,H $\alpha$ ,S1
8	22 59 36.51	-34 43 25.4	20.2		20.3	0.38058	0.00022		em:H $\alpha$ ,S1
9	22 59 25.99	-34 43 31.9				0.21032?			very uncertain
10	22 59 18.60	-34 43 43.6	20.5	18.8	18.9	0.21940	0.00024	4.76	em:H $\alpha$ ,S1 65840 km s $^{-1}$
11	22 59 17.61	-34 43 57.1			19.3	0.31185	0.00019	3.27	
12	22 59 20.05	-34 44 09.4	20.8	19.5	18.2	0.22127	0.00012	3.56	em:H $\beta$ ,H $\alpha$ 66509 km s $^{-1}$
13	22 59 20.00	-34 44 20.3			20.0	0.40980	0.00028	4.48	
15	22 59 28.09	-34 44 29.0			19.4	0.07309	0.00045		em:H $\beta$ ,2OIII,H $\alpha$
16	22 59 28.82	-34 44 44.1			18.6	0.40823	0.00029	3.61	
17	22 59 38.42	-34 44 52.4			20.5	0.34606	0.00029	3.04	very weak
18	22 59 23.15	-34 45 03.0			19.7	0.31301	0.00007		em:H $\alpha$ ,S1
19	22 59 18.51	-34 45 13.1	21.2	20.3	19.6	0.40876	0.00022		em:OII,H $\beta$ ,2OIII,H $\alpha$ ,S1
20	22 59 40.37	-34 45 21.8			18.1	0.23192	0.00018	5.23	
22	22 59 24.80	-34 45 36.6	22.3	19.6	18.8	0.41015	0.00025	5.19	em:H $\beta$ ,H $\alpha$
24	22 59 28.59	-34 45 49.8	21.6	19.6	18.9	0.33369	0.00018	4.84	em:OII
25	22 59 35.08	-34 45 57.0	22.4		20.9	0.32344	0.00028	3.12	
26	22 59 32.09	-34 46 13.6			19.6	0.40926	0.00027	3.65	
27	22 59 32.34	-34 46 23.3			19.9	0.46615	0.00022	3.22	
28	22 59 26.16	-34 46 32.5	20.2	19.2	19.0	0.35118	0.00028	3.11	weak
30	22 59 36.18	-34 46 43.1	20.8	18.8	19.6	0.31860	0.00033	3.15	
31	22 59 33.65	-34 46 49.2			19.9	0.33342			measured on H $\alpha$
34	22 59 25.25	-34 47 05.9			20.0	0.32794	0.00042	3.02	very weak
36	22 59 34.22	-34 47 19.9			19.6	0.33300	0.00027	3.12	very weak
37	22 59 23.76	-34 47 27.4	21.0	19.8	19.6	0.31604	0.00004		em:H $\beta$ ,2OIII,H $\alpha$ ,S1
38	22 59 18.07	-34 47 39.8			19.9	0.30236	0.00016	3.10	
40	22 59 23.41	-34 47 57.6	20.6	18.9	18.1	0.32283	0.00027	3.37	em:H $\beta$ ,2OIII,H $\alpha$ ,S1: 96857 km s $^{-1}$
41	22 59 16.77	-34 48 06.8			20.0	0.32061	0.00045		
44	22 59 15.92	-34 48 43.8	22.2	21.1	19.1	0.28628?	0.00060	4.04	uncertain
45a	22 59 31.40	-34 48 50.3				0.35159			measured on H $\alpha$ ,S1
45b	22 59 31.40	-34 48 50.4				0.34461			measured on H $\alpha$ ,S1
Quadrant 2									
1a	22 59 16.30	-34 33 40.6	20.8	19.0	19.6	0.25782	0.00023	3.43	em:H $\beta$ ,2OIII,H $\alpha$
1b	22 59 16.30	-34 33 40.6				0.33069	0.00024	3.18	em:H $\alpha$ , 2 galaxies
2	22 59 18.23	-34 33 50.7			18.2	0.49578	0.00029		em:OII,H $\beta$ ,2OIII,H $\alpha$ ,S1
3	22 59 18.00	-34 33 58.5			20.5	0.41000	0.00033		em:OII,H $\beta$ ,2OIII,H $\alpha$
4	22 59 13.67	-34 34 11.1			19.3	0.40846	0.00033		em:H $\beta$ ,2OIII
5	22 59 15.03	-34 34 23.5	22.5	20.1	18.8	0.41440	0.00034	3.01	very uncertain
6	22 59 23.91	-34 34 32.7	21.3	19.2	18.9	0.42284	0.00021	6.45	
7	22 59 21.45	-34 34 41.8			18.6	0.23156	0.00024	3.36	very weak
8	22 59 12.89	-34 34 48.4			21.2	0.44924	0.00018	3.03	weak
9	22 59 17.73	-34 34 54.1			20.9	0.31359?			very uncertain
10	22 59 18.77	-34 35 02.2	21.5	19.9	19.5	0.40848	0.00023	3.36	
11	22 59 16.88	-34 35 08.5			17.6	0.34546			measured on H $\alpha$
12	22 59 32.84	-34 35 24.7	21.9		19.2	0.34646	0.00021	3.08	em:H $\alpha$
13	22 59 26.31	-34 35 32.2			17.8	0.27013	0.00038	3.52	very weak
14	22 59 20.21	-34 35 43.7			18.7	0.37370	0.00009		em:OII,H $\alpha$ ,S1
15	22 59 15.61	-34 35 51.1			20.7	0.41045	0.00026	4.01	
16	22 59 19.18	-34 35 59.7	21.4	20.4	19.7	0.34469	0.00021	3.41	
18	22 59 12.16	-34 36 28.0	21.0		19.4	0.38110	0.00042	4.03	
19	22 59 19.31	-34 36 38.6	22.00	20.1	18.8	0.37706	0.00021	6.71	
21	22 59 21.69	-34 36 53.5			19.2	0.41304	0.00020	6.52	
22	22 59 36.79	-34 36 53.5			21.3	0.39104			em:H $\alpha$
23	22 59 21.57	-34 37 07.8	19.3	18.4	18.3	0.41310	0.00022	6.81	
24	22 59 36.81	-34 37 21.2			19.2	0.37972	0.00052		em:OII,H $\beta$ ,2OIII

Gal.	R.A. (J2000)	Dec. (J2000)	$B_j$ mag	$R_f$ mag	$R_{\text{comp}}$ mag	redshift	error	R	notes
26	22 59 12.34	-34 37 37.5	22.3	20.2	19.4	0.48676	0.00018		em:OII,H $\beta$ ,2OIII
27	22 59 21.00	-34 37 46.0	20.6	20.0	19.9	0.49642	0.00024	4.53	
28	22 59 15.56	-34 37 57.2	20.8	19.4	19.7	0.47064	0.00027	3.16	
29	22 59 17.62	-34 38 03.8			20.9	0.39781	0.00055	3.06	very weak, uncertain
31	22 59 24.67	-34 38 18.4	21.4	20.6	18.5	0.49717	0.00016		em:OII,H $\beta$ ,2OIII,H $\alpha$
32	22 59 25.00	-34 38 35.6	20.8	19.5	19.5	0.30913	0.00028		em:H $\beta$ ,2OIII,H $\alpha$
33	22 59 16.65	-34 38 43.7	20.1	18.1	20.4	0.46922	0.00051	3.17	em:H $\beta$ 140472 km s <sup>-1</sup>
35	22 59 40.57	-34 39 05.1			19.7	0.31290	0.00016	7.72	
36	22 59 25.79	-34 39 11.8	21.4	20.0	19.8	0.46367	0.00020	6.71	
37	22 59 13.94	-34 39 33.0	21.8	20.7	18.7	0.32064	0.00016	3.42	
38	22 59 23.08	-34 39 47.1			20.1	0.29869	0.00017		em:H $\beta$ ,2OIII,H $\alpha$ ,S1
39	22 59 39.01	-34 39 53.1			20.6	0.37203	0.00012		em:OII,H $\beta$ ,2OIII,H $\alpha$
40	22 59 36.39	-34 39 58.4			20.3	0.41913	0.00023	4.96	
41	22 59 43.80	-34 40 06.7			20.5	0.31907	0.00026	3.08	
Quadrant 3									
1	22 58 41.57	-34 33 18.1	20.3	18.8	19.8	0.32951	0.00015		em:H $\beta$ ,2OIII,H $\alpha$ ,S1
2	22 58 41.21	-34 33 27.8	20.5	18.8	18.7	0.33307	0.00011		em:H $\beta$ ,2OIII,H $\alpha$ ,S1
3	22 58 40.11	-34 33 34.6	21.9	19.2	19.4	0.33127	0.00024	5.48	
4	22 58 40.08	-34 33 42.2	21.3	19.9	20.0	0.21259	0.00019		em:H $\beta$ ,2OIII,H $\alpha$ ,S1
5	22 58 41.10	-34 33 49.0			20.5	0.33189	0.00020		em:H $\beta$ ,2OIII,H $\alpha$ ,S1
6	22 58 33.87	-34 33 53.5			19.2	0.38938?			uncertain
8	22 58 42.73	-34 34 23.0	22.0		19.7	0.39969	0.00028	3.48	em:H $\alpha$ :119724 km s <sup>-1</sup>
10	22 58 22.64	-34 34 33.3	19.8	18.7	18.8	0.31365	0.00012	4.63	
11	22 58 35.95	-34 34 45.6	22.4	20.6	20.1	0.21245	0.00026		em:H $\beta$ ,2OIII,H $\alpha$ ,S1
12	22 58 36.88	-34 34 58.2	21.5	19.6	19.0	0.30939	0.00009		em:H $\beta$ ,2OIII,H $\alpha$ ,S1
13	22 58 51.29	-34 35 07.6			19.3	0.36347	0.00044	3.02	very weak
15	22 58 41.00	-34 35 21.4			20.3	0.47562	0.00038	3.01	very weak
16	22 58 45.84	-34 35 30.4	20.9	20.4	20.0	0.17739	0.00012		em:H $\beta$ ,2OIII,H $\alpha$ ,S1
17	22 58 48.43	-34 35 39.7			20.1	0.31846	0.00041	3.22	
18	22 58 56.50	-34 35 48.2	20.8	19.3	19.5	0.22176	0.00009		em:H $\beta$ ,2OIII,H $\alpha$ ,S1
19	22 58 23.26	-34 35 57.0	20.0	18.6	18.9	0.15860	0.00015	4.84	
20	22 58 32.46	-34 36 07.9			19.2	0.32601	0.00029	3.01	very weak
21	22 58 32.39	-34 36 15.5	21.1	19.2	20.8	0.35231	0.00021		em:H $\beta$ ,H $\alpha$ ,S1,S2
23	22 58 22.99	-34 36 26.7	22.1	20.5	20.5	0.43221	0.00036	3.39	
24	22 58 28.94	-34 36 34.7			18.2	0.30386	0.00045	3.01	very weak
25	22 58 40.69	-34 36 41.1			20.1	0.47190	0.00039	3.15	
26	22 58 28.24	-34 36 48.7			20.2	0.31477	0.00024	4.07	
27	22 58 29.50	-34 36 55.9			19.6	0.41028?			uncertain
28	22 58 24.28	-34 37 02.1			18.4	0.25761	0.00018	5.51	
29	22 58 32.32	-34 37 07.5	21.6	20.1	20.6	0.47283	0.00038	3.15	
30	22 58 27.93	-34 37 16.9	21.2	20.1	21.1	0.40221	0.00023		em:OII, H $\beta$ ,2OIII,H $\alpha$
31	22 58 44.38	-34 37 24.2	22.2	20.2	20.1	0.39764	0.00040	3.04	em:H $\beta$ ,H $\alpha$
33	22 58 39.09	-34 37 52.3			18.8	0.34480			measured on H $\alpha$
34	22 58 39.66	-34 38 03.8			20.1	0.35179	0.00011		em:OII,H $\beta$ ,2OIII,H $\alpha$ ,S1
35	22 58 33.67	-34 38 18.9	21.4	20.1	18.9	0.43091	0.00014		em:H $\beta$ ,2OIII,H $\alpha$ ,S1
36	22 58 31.51	-34 38 24.2	22.3	20.7	20.5	0.20326	0.00031		em:H $\alpha$ ,S1
38	22 58 41.21	-34 38 40.5			19.3	0.43205	0.00029	3.58	em: OII
39	22 58 46.63	-34 38 45.7	21.9	20.6	20.2	0.39935	0.00011		em:OII,H $\beta$ ,2OIII,H $\alpha$ ,S1
40	22 58 34.07	-34 38 53.1	21.9	19.9	19.3	0.31828	0.00031	4.12	
43	22 58 39.42	-34 39 13.5			20.2	0.27849	0.00033	3.11	
44	22 58 39.45	-34 39 24.1	22.2	19.4	19.5	0.22464	0.00017	3.34	em: H $\alpha$ ,S1 67344 km s <sup>-1</sup>
45	22 58 43.50	-34 39 32.3	21.6	20.6	20.1	0.32099	0.00020	3.07	
46	22 58 42.70	-34 39 40.6			20.4	0.32952	0.00034	3.02	very weak
49	22 58 37.09	-34 40 06.8	19.4	18.2	18.9	0.20657	0.00019	4.82	em:H $\alpha$ ,S1 61753 km s <sup>-1</sup>
Quadrant 4									
2	22 58 34.99	-34 42 24.0			19.5	0.31982	0.00035	5.82	em:H $\alpha$ weak
3	22 58 45.17	-34 42 28.9	22.6	19.1	20.1	0.32038	0.00021	3.18	
4	22 58 35.53	-34 42 35.8			19.7	0.31108	0.00014	3.42	

Gal.	R.A. (J2000)	Dec. (J2000)	$B_j$ mag	$R_f$ mag	$R_{\text{comp}}$ mag	redshift	error	R	notes
5	22 58 42.57	-34 42 42.5			20.6	0.42558	0.00012		em:H $\beta$ ,2OIII,H $\alpha$ ,S1
7	22 58 32.37	-34 42 55.1	20.4	19.7	20.0	0.16952	0.00009		em:H $\beta$ ,2OIII,H $\alpha$ ,S1
8	22 58 32.75	-34 43 02.0			19.5	0.17061	0.00022		em:H $\beta$ ,2OIII,H $\alpha$ ,S1
9a	22 58 31.70	-34 43 18.8	21.0	18.9	18.4	0.29095	0.00009	10.95	
9b	22 58 31.70	-34 43 18.8				0.25733			em:H $\alpha$
10	22 58 25.31	-34 43 25.5	20.5	18.8	19.5	0.31228			em:H $\alpha$ very weak
11	22 58 32.43	-34 43 30.3	19.0	17.4	20.0	0.30473	0.00008	3.02	very weak
12	22 58 26.84	-34 43 34.1	22.1	21.0	19.7	0.31166	0.00026	3.05	
13	22 58 26.64	-34 43 44.0	22.4	20.5	20.9	0.47564	0.00016	3.40	
14	22 58 41.60	-34 43 46.5	20.5	18.9	20.7	0.30460	0.00007		em:OII,H $\beta$ ,2OIII,H $\alpha$ ,S1
15	22 58 25.91	-34 43 52.0	21.2	19.8	20.9	0.30799	0.00030		em:H $\beta$ ,2OIII
16	22 58 29.50	-34 43 55.5	22.2	19.8	20.4	0.31854	0.00035	3.52	
18	22 58 25.81	-34 44 06.4			20.6	0.32247	0.00029	3.19	
19	22 58 26.24	-34 44 12.1			20.2	0.31070	0.00011		em:H $\beta$ ,2OIII,H $\alpha$ ,S1
20	22 58 39.44	-34 44 18.6			19.6	0.30863	0.00011		em:H $\beta$ ,2OIII,H $\alpha$ ,S1
21	22 58 50.72	-34 44 16.7			19.5	0.30605	0.00024	4.32	
22	22 58 39.87	-34 44 28.0			19.4	0.31445	0.00022	5.69	
23	22 58 35.11	-34 44 34.8	21.9		20.6	0.32268	0.00030	3.09	
24	22 58 33.19	-34 44 39.7			20.5	0.31448	0.00028	3.12	
25	22 58 30.22	-34 44 42.4			19.4	0.30132	0.00035	3.20	
26	22 58 42.00	-34 44 51.2	20.6	18.9	18.9	0.32462	0.00012		em:OII,H $\beta$ ,2OIII,H $\alpha$ ,S1
27	22 58 29.86	-34 44 55.5			21.4	0.31265	0.00023	3.08	
28	22 58 26.83	-34 45 02.6			20.0	0.31467	0.00032	3.53	
31	22 58 36.47	-34 45 17.4	21.0	19.3	19.1	0.31779	0.00024	5.33	
32	22 58 38.00	-34 45 24.1	20.2	17.7	18.2	0.31708	0.00024	5.65	
33	22 58 41.30	-34 45 30.6	21.1	19.6	19.8	0.10193	0.00029		em:OII,H $\beta$ ,2OIII,H $\alpha$ ,S1
35	22 58 47.92	-34 45 45.0	21.7	19.5	20.2	0.17040	0.00011		em:H $\beta$ ,2OIII,H $\alpha$ ,S1
36	22 58 35.91	-34 45 50.1	19.8	17.7	18.4	0.31307	0.00019	5.65	
37	22 58 29.65	-34 45 57.5			19.1	0.17051	0.00018	3.01	uncertain
38	22 58 28.42	-34 46 02.3	22.0	19.8	19.2	0.30100	0.00026	5.63	
39	22 58 38.57	-34 46 10.7			20.1	0.32594	0.00047	3.43	
40	22 58 24.92	-34 46 18.7	20.8	19.0	19.0	0.31779	0.00004		em:H $\alpha$
41	22 58 27.85	-34 46 26.3			19.7	0.31816	0.00033	4.55	
42	22 58 29.75	-34 46 32.1	22.2	20.5	19.9	0.50228	0.00035	3.04	
43	22 58 28.88	-34 46 40.3			20.2	0.31717	0.00033	3.68	
44	22 58 40.93	-34 46 45.7	20.6	18.6	18.3	0.31523	0.00030	4.73	
45	22 58 36.47	-34 46 51.2			20.6	0.31389	0.00019	4.66	
46	22 58 51.00	-34 47 00.6	20.8	19.5	20.1	0.32953	0.00028	3.10	
47	22 58 34.80	-34 47 07.1	22.2		19.3	0.31674	0.00019	6.24	
48	22 58 29.14	-34 47 13.1	21.6	20.0	20.0	0.31462	0.00022	5.29	
49	22 58 39.56	-34 47 17.4	21.8	19.1	20.0	0.31818	0.00024	4.89	
50	22 58 48.11	-34 47 21.3			20.2	0.33032	0.00039	3.02	very weak
51	22 58 46.31	-34 47 31.5	20.8	18.8	19.1	0.30954	0.00019	6.32	
52	22 58 26.11	-34 47 37.5	22.6	20.9	18.2	0.38782	0.00037	3.04	very weak
54	22 58 33.80	-34 47 46.6	22.3	19.5	18.9	0.34779	0.00030	3.06	weak
55a	22 58 33.96	-34 47 53.3			20.2	0.31776	0.00031	3.26	
55b	22 58 33.96	-34 47 53.3				0.17199			em:H $\beta$ ,2OIII,H $\alpha$ ,S1
56	22 58 44.05	-34 47 59.4			18.4	0.32814	0.00044	3.31	
57	22 58 49.74	-34 48 01.9	21.6	19.7	19.1	0.31451	0.00028	3.35	
58	22 58 41.65	-34 48 06.7	21.9	19.2	19.2	0.31082	0.00028	6.10	
59	22 58 45.48	-34 48 14.9			20.1	0.31831	0.00035	3.04	weak
60	22 58 44.45	-34 48 21.3			19.0	0.32473	0.00031	4.42	
61	22 58 38.22	-34 48 27.8	20.7	18.6	19.7	0.72072	0.00014	3.05	
62	22 58 42.81	-34 48 33.4	21.0	18.9	29.9	0.31090	0.00047	5.43	
63	22 58 52.67	-34 48 39.1			20.2	0.31874	0.00024	4.98	
64	22 58 31.46	-34 48 53.3			18.3	0.31447	0.00030	5.28	
65	22 58 34.69	-34 49 01.3			20.6	0.47788	0.00023	5.33	

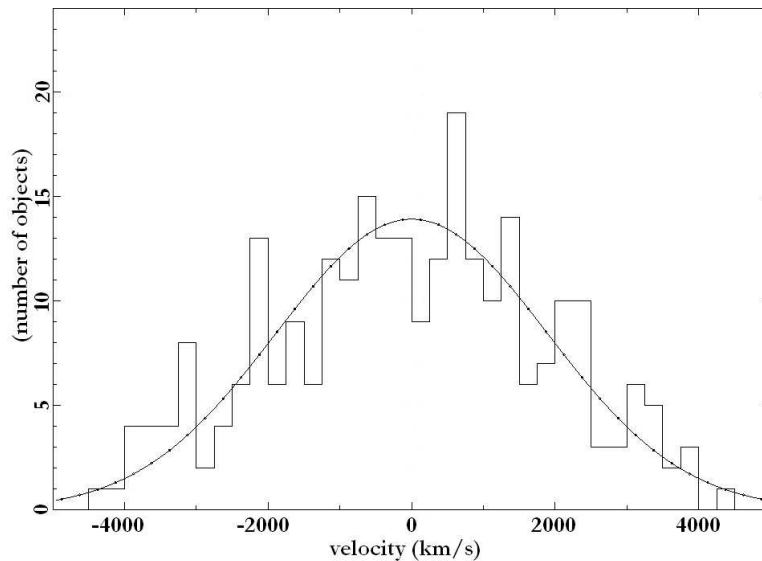


**Figure 8.** Rest-frame histogram of the velocity distribution of the AC114 cluster between 89000 and 101000  $\text{km s}^{-1}$  with a step of  $250 \text{ km s}^{-1}$ ; the gaussian with  $\sigma = 1893 \text{ km s}^{-1}$  (rest-frame) is also shown.

**Table 3.** Positions and redshifts of foreground, main and distant background structures of AC114.

Ident	R.A.	Dec	$z_{\text{cl}}$	$N_{\text{gal}}$	$N_{\text{gal}}^{(a)}$	Probability
				0.5/h Mpc	2.5/h Mpc	
AC114 main	22 58 45.6	-34 48 00	0.317242	98	177	0.99
AC114 01	22 58 43.0	-34 46 34	0.301921	4	17	0.77
AC114 02	22 59 06.2	-34 46 16	0.409360	3	$10^{(b)}$	0.60

<sup>a</sup> After running the shifting gapper procedure to remove interlopers.

<sup>b</sup> Not confirmed by shifting gapper.

ellipsoid of semi-major axis  $r_{200}$  is 200 times the critical density at the halo redshift. This method yielded a mass estimate  $M_{200} = (1.3 \pm 0.9) \times 10^{15} M_{\odot}/h$ .

De Filippis et al. (2004) derives X-ray masses from *Chandra* images with:

$$M_{\text{tot}}(1\text{Mpc}) = (4.5 \pm 1.1) \times 10^{14} \times h_{72}^{-1} M_{\odot}$$

$$M_{\text{gas}}(1\text{Mpc}) = (8.4 \pm 2.6) \times 10^{13} \times h_{72}^{-5/2} M_{\odot}$$

They compare their mass estimates with those obtained from weak - and strong lensing by Natarajan et al. (1998) and conclude that they are in remarkably good agreement. Table 4 summarizes the available mass estimates from Natarajan et al. (1998), De Filippis et al. (2004), Sereno et al. (2010) and the present work, in units of  $10^{14} M_{\odot}$  as a function of the radius in Mpc; the method used for mass determination is also indicated. We note that, despite the fact the mass determinations are made with a wide range of radial extents, they all appear to be fairly robust measurements with small relative errors, independent of the method used. If systematic biases exist, they have a weak influence on the results. As quoted in Biviano et al. (2006), projection effects have a significant impact on the reliability of cluster mass estimates through the inclusion of interlopers among the samples of presumed cluster members. In the present work we have only considered galaxies that are securely members of the main cluster and located inside the

Abell radius. The presence of one foreground structure along the line-of-sight may lead to a higher level of uncertainty in the mass estimate presented.

## 7 SUMMARY AND CONCLUSIONS

- We have presented a dynamical analysis of the galaxy cluster AC114 based on a catalogue of 524 velocities of which 169 (32%) are newly obtained at the European Southern Observatory with the VLT and the VIMOS spectrograph.

- We obtained an improved mean redshift value  $z = 0.31665 \pm 0.0008$  and velocity dispersion  $\sigma = 1893_{-82}^{+73} \text{ km s}^{-1}$ . The cluster has a very elongated main radial filament spanning  $12000 \text{ km s}^{-1}$  in redshift space.

- Using Katgert et al. (1996) method, we have been able to detect two secondary structures although at low level of significance. A radial foreground one is detected within the central 0.5/h Mpc radius, recognizable as a redshift group at the same central redshift value. The galaxies taking part of a background structure are sparsely distributed background to the main AC114, so that no conclusion can be given on a bound structure.

- AC114 is an archetype Butcher-Oemler galaxy cluster. We analyzed the color distribution for this galaxy cluster

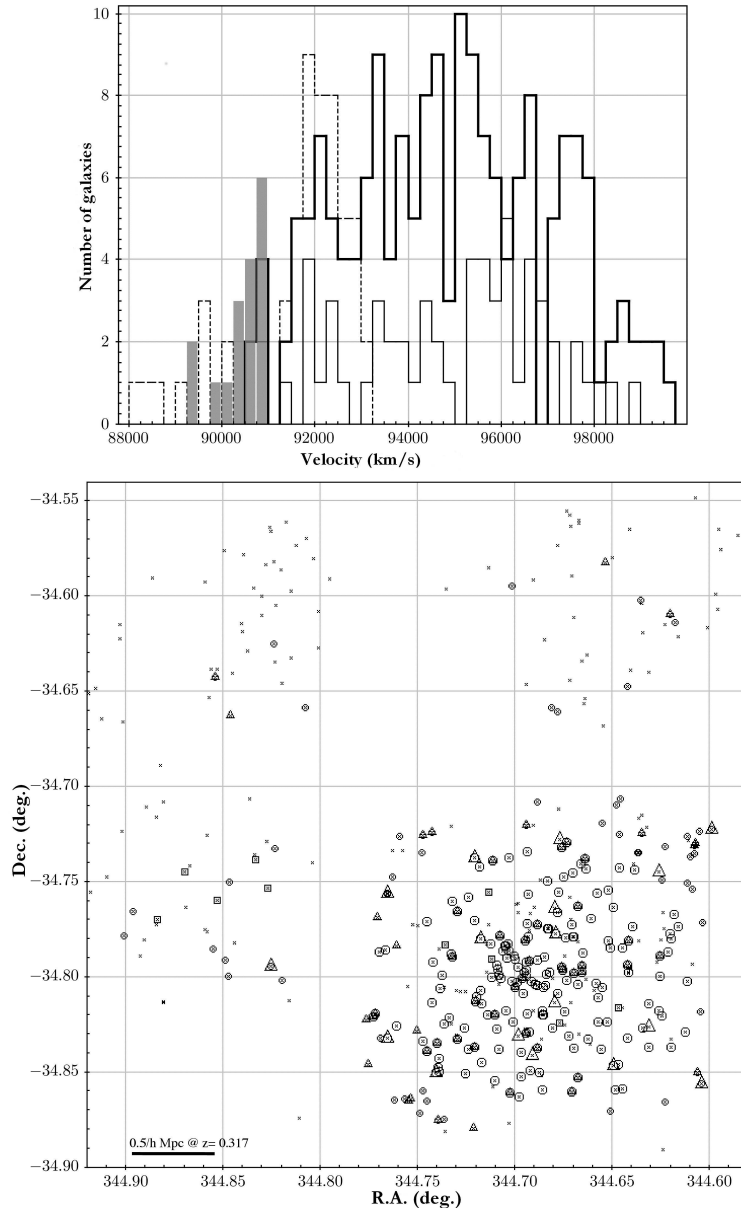


**Figure 9.** *upper panel:* Velocity histogram (step= 250 km s<sup>-1</sup>) showing the main (heavy stepped line) and foreground (filled rectangles) structures detected as described in the text. The *light stepped lines* show the distribution of galaxies classified as interlopers for each of the structures. *Lower panel:* the projected distribution of galaxies of our spectroscopic sample (*small crosses*); *large/small open circles* show the positions of the galaxies belonging/interlopers to the main cluster, *large/small open triangles* give the positions of the foreground/interlopers structures galaxies and *small/open squares* are for those belonging to the background structure (cf. Table 3).

and identify the sequence of red galaxies which is well separated from the blue galaxies. The latter subset contains 44% of confirmed members of the cluster, reaching magnitudes as faint as  $R_f = 21.1$  (1.0 magnitude fainter than previous studies).

- From the spectroscopic data for  $N = 265$  galaxies cluster members we derive a dynamical mass  $M_{200} = (4.3 \pm 0.7) \times 10^{15} M_{\odot}/h$  for AC114 and  $M_v = (5.4 \pm 0.7 \pm 0.6) \times 10^{15} M_{\odot}/h$  from the intrinsic velocity dispersion out to a radius of 3.98/h Mpc.

The next phase of this study of AC114 will be to obtain direct metallicities of emission-line galaxies (Saviane et al.

2014). The redshift of AC114 puts it near the limit where VIMOS can be used to derive oxygen abundances via the  $T_e$  method, and this cluster is a well-known gravitational lens, with a number of photometric data sets already existing. At such a redshift, all important emission lines still fall in the optical range, and the Universe is  $\approx 70\%$  its current age, so we can expect a factor 1.4 increase in  $Z$  since that time, or 0.14 dex in  $[m/H]$ . A preliminary presentation of our metallicity analysis can be seen in Saviane et al. (2014).

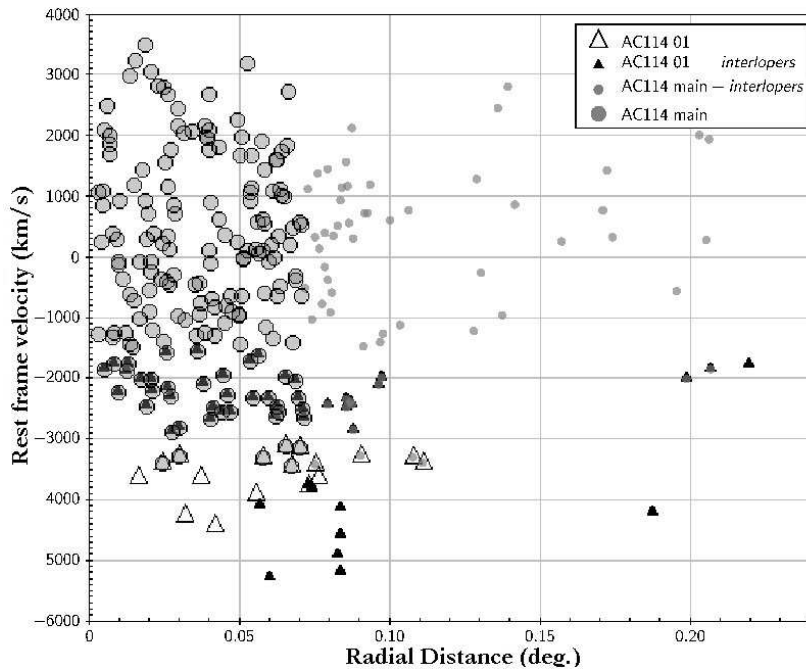


**Figure 10.** Relative velocity with respect to the mean cluster velocity plotted against angular distance  $R$  from the projected cluster center for the galaxies around the cluster velocity. The left axis expresses relative velocity with respect to the mean velocity of the cluster; symbols are identical to Fig.9.

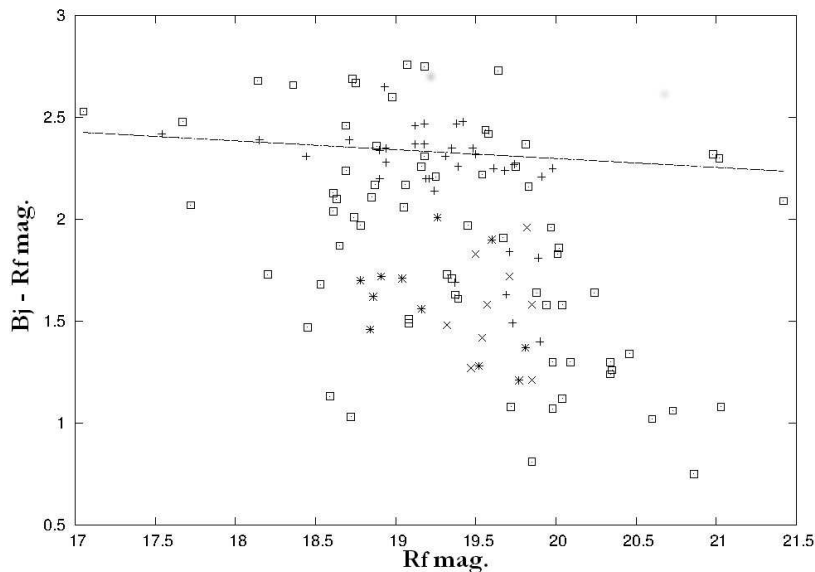


**Figure 11.** the  $B_j - R_f$  diagram as a function of  $R_f$  for the AC114 cluster member galaxies within an Abell radius of 5.3 arcmin. (+) and (x) correspond respectively to absorption and emission-lines galaxies observed by Couch & Sharples (1987), while squares and (\*) are absorption and emission-lines galaxies from our spectroscopic sample.

## ACKNOWLEDGEMENTS

We thank ESO-VLT staff for their assistance during the observations (program ID 083.A-0566A), and DP thanks ESO in the context of the *Visiting Scientists program* for its hospitality at Santiago (Chile). We also thank the referee for their very advised comments.

## REFERENCES

- Abell G.O., Corwin H.G., Olowin R.P., 1989, ApJS, 70, 1
- Adami C., Mazure A., Biviano A., Katgert P., Rhee G., 1998, A&A, 331, 439
- Allen S.W., 1998, MNRAS, 296, 392
- Allen S.W., 2000, MNRAS, 315, 269
- Beers T.C., Flynn K., Gebhardt K., 1990, AJ, 100, 32
- Binney J., Tremaine S., 1987, Galactic dynamics. Princeton

□

**Table 4.** AC114 mass determinations as a function of the radius with different methods.

Radius (Mpc)	mass $10^{14}M_{\odot}/h$	error bar	reference	method
0.075	0.42	0.01	Natarajan et al. (1998)	lensing
0.075	0.44	0.06	De Philippis et al. (2004)	X-ray
0.075	0.40	0.03	Sereno et al. (2010)	ICM, gal. halos, DM
0.150	1.20	0.15	Natarajan et al. (1998)	lensing
0.150	1.12	0.17	De Philippis et al. (2004)	X-ray
0.150	1.12	0.09	Sereno et al. (2010)	ICM, gal. halos, DM
0.500	4.0	0.04	Natarajan et al. (1998)	lensing
0.500	4.7	0.10	De Philippis et al. (2004)	X-ray
1.000	4.5	0.11	De Philippis et al. (2004)	$M_{tot}$
3.98	34.0	8.0	Sereno et al. (2010)	Virial
3.98	43.0	7.0	this work	Virial
3.98	48.0	8.0	Sereno et al. (2010)	Biviano et al. (2006)
3.98	54.0	7.0	this work	Biviano et al. (2006)

- Univ. Press, Princeton, NJ
- Biviano A., Murante G., Borgani S., Diaferio A., Dolag K., Girardi M., 2006, *A&A*, 456, 23
- Butcher H., Oemler A., 1978, *ApJ*, 219, 18
- Campusano L.E., Pellò R., Kneib J.P., Le Borgne J.F., Fort B., Ellis R.S., Mellier Y., Smail Y., 2001, *A&A*, 378, 394
- Colless M., Peterson B.A., Jackson C., Peacock J.A., Cole S., Norberg P., Baldry I.K., Baugh C.M., Bland-Hawthorn J., Bridges T., Cannon R., Collins C., Couch W., Cross N., Dalton G., De Propris R., Driver S.P., Efstathiou G., Ellis R.S., Frenk C.S., Glazebrook K., Lahav O., Lewis I., Lumsden S., Maddox S., Madgwick D., Sutherland W., Taylor K., 2003, preprint (arXiv:0306581)
- Couch W.J., Sharples R.M., 1987, *MNRAS*, 229, 423
- Couch W.J., Barger A.J., Smail I., Ellis R.S., Sharples R.M., 1998, *ApJ*, 497, 518
- Couch W.J., Balogh M.I., Bower R.G., Smail I., Glazebrook K., Taylor M., 2001, *ApJ*, 549, 820
- Cypriano E.S., Lima Neto G.B., Sodré Jr. L., Kneib J.P., Campusano L.E., 2005, *ApJ*, 630, 38
- Czoske O., Kneib J.P., Soucail G., Bridges T.J., Mellier Y., Cuillandre J.C., 2001, *A&A*, 372, 391
- Czoske O., Moore B., Kneib J.P., Soucail G., 2002, *A&A*, 386, 31
- De Filippis E., Bautz M.W., Sereno M., Garmire G.P., 2004, *ApJ*, 611, 164
- Diaferio A., Geller M.J., 1997, *ApJ*, 481, 633
- Diaferio A., Kauffmann G., Balogh M. L., White S. D. M., Schade D., Ellingson E., 2001, *MNRAS*, 323, 999
- Dressler A., Shectman S.A., 1988, *AJ*, 95, 284
- Fadda D., Girardi M., Giuricin G., Mardirossian F., Mezzetti M., 1996, *ApJ*, 473, 670
- Feigelson E.D., Babu G.J., 2013, *Modern Statistical Methods for Astronomy*, Cambridge University Press
- Finn R.A., Zaritski D., McCarthy Jr. D.W.: 2004, *ApJ*, 604, 141
- Girardi M., Giuricin G., Mardirossian F., Mezzetti M., Boschini W., 1998, *ApJ*, 505, 74
- Gulliesz M., Held E.V., Saviane I., Rizzi L., 2009, *A&A*, 500, 735
- Hambly N.C., Irwin M.J., MacGillivray H.T., 2001, *MNRAS*, 326, 1295
- Hamuy M., Walker A.R., Suntzeff N.B., Gigoux P., Heathcote S.R.; Phillips M.M., 1992, *PASP*, 104, 553
- Hamuy M., Suntzeff N.B., Heathcote S.R., Walker A.R., Gigoux P., Phillips M.M., 1994, *PASP*, 106, 566
- Jones D.H., Read M.A., Saunders W., Colless M., Jarrett T., Parker Q.A., Fairall A.P., Mauch T., Sadler E.M., Watson F.G., Burton D., Campbell L.A., Cass P., Croom S.M., Dawe J., Fiegert K., Frankcombe L., Hartley M., Huchra J., James D., Kirby E., Lahav O., Lucey J., Mamon G.A., Moore L., Peterson B.A., Prior S., Proust D., Russell K., Safouris V., Wakamatsu K., Westra E., Williams M., 2009, *MNRAS*, 399, 683
- Just D.W., Zaritsky D., Desai V., Rudnick G., 2010, *ApJ*, 711, 192
- Katgert P., Mazure A., Perea J., den Hartog R., Moles M., Le Fevre O., Dubath P., Focardi P., Rhee G., Jones B., Escalera E., Biviano A., Gerbal D., Giuricin G., 1996, *A&A*, 310, 8
- Kent S.M., Gunn J.E., 1982, *AJ*, 87, 945
- Kurtz M.J., Mink D.J., Wyatt W.F., Fabricant D.G., Torres G., Kriss G.A., Tonry J.L., 1991, *Astron. Soc. Pacific Conf. Ser.*, 25, 432
- Larson R.B., 1974, *MNRAS*, 169, 229
- Leccardi A., Molendi S., 2008, *A&A*, 486, 359
- Leaman Ryan., Venn K.A., Brooks A.M., Battaglia G., Cole A., Ibata R.A., Irwin M.J., McConnachie A.W., Mendel J.T., Starkeburg E., Tolstoy E., 2013, *ApJ*, 767, 131
- Le Fèvre O., Crampton D., Lilly S.J., Hammer F., Tresse L., 1995, *ApJ*, 455, 60
- Le Fèvre O., Saisse M., Mancini D., Brau-Nogue S., Caputi O., Castinel L., D'Odorico S., Garilli B., Kissler-Patig M., Lucuix C., Mancini G., Pauget A., Sciarretta G., Scodreggio M., Tresse L., Vettolani G., 2003, *Proc. SPIE*, 4841, 1670
- Lopes P.A.A., de Carvalho R.R., Kohl-Moreira J.L., Jones C., 2009, *MNRAS*, 399, 2201
- Maddox S.J., Sutherland W.J., Efstathiou G., Loveday J., 1990, *MNRAS*, 243, 692
- Maddox S.J., Efstathiou G., Sutherland W.J., 1990, *MNRAS*, 246, 433
- Mahdavi A., Geller M.J., 2001, *ApJ*, 554, L129
- Martini P., Kelson D.D., Kim E., Mulchaey J.S., Athey A.A., 2006, *ApJ*, 644, 116



- Martini P., Mulchaey J.S., Kelson D.D., 2007, *AJ*, 664, 761  
Mellier Y., 1999, *ARA&A*, 37, 127  
Mink D.J., Wyatt W.F., 1995, in Shaw R. A., Payne H. E., Hayes J. J. E., eds, *ASP Conf. Ser. Vol. 77, Astronomical Data Analysis Software and Systems IV*. Astron. Soc. Pac., San Francisco, p. 496  
Natarajan P., Kneib J.P., Smail I., Ellis R.S., 1998, *ApJ*, 499, 600  
Pickles A.J., 1985, *ApJS*, 59, 33  
Pickles A.J., 1998, *PASP*, 110, 863  
Regos E., Geller M.J., 1989, *AJ*, 98, 755  
Reisenegger A., Quintana H., Carrasco E.R., Maze J., 2000, *AJ*, 120, 523  
Ribeiro A.L.B., de Carvalho R.R., Trevisan M., Capelato H.V., La Barbera F., Lopes P.A.A., Schilling A.C., 2013, *MNRAS*, 434, 784  
Rood H.J., Page T.L., Kintner E.C., King I.R., 1972, *ApJ*, 175, 627  
Saviane I., Yegorova I., Proust D., Bresolin F., Ivanov V., Held E.V., Salzer J., Rich R.M., 2014, *Mem. S. A. I. Vol. 85*, p. 417  
Serenio M., Lubini M., Jetzer Ph., 2010, *A&A*, 518, 55  
Smail I., Couch W.J., Ellis R.S., Sharples R.S., 1995, *ApJ*, 440, 501  
Tonry J., Davis M., 1979, *AJ*, 84, 1511  
2011, *A&A*, 532, 105  
ZuHone J.A., Ricker P.M., Lamb D.Q., Karen Yang H.Y., 2009, *ApJ*, 699, 1004